Heterogeneous Oxysulfide@Fluoride Core/Shell Nanocrystals for Upconversion-Based Nanothermometry

Qilin Zou, Cécile Marcelot, Nicolas Ratel-Ramond, Xiaodong Yi, Pierre Roblin, Florian Frenzel, Ute Resch-Genger, Ali Eftekhari, Aude Bouchet, Christophe Coudret, et al.

Heterogeneous oxysulfide@fluoride core/shell nanocrystals for upconversion-based nanothermometry

Qilin Zou,[#,†] *Cécile Marcelot,*[†] *Nicolas Ratel-Ramond,*[†] *Xiaodong Yi,*[||] *Pierre Roblin,*[°] *Florian Frenzel,*[§] *Ute Resch-Genger,*[§] *Ali Eftekhari,*[‡] *Aude Bouchet,*[‡] *Christophe Coudret,*[#] *Marc Verelst,*[†] *Xueyuan Chen,*[*,||] *Robert Mauricot,*[*,†] *and Clément Roux*[*,#]

#Laboratoire des IMRCP, CNRS UMR 5623, Université de Toulouse - UPS, 118 route de Narbonne, 31062 Toulouse Cedex 09, France

†Centre d'Elaboration des Matériaux et d'Etudes Structurales, CNRS, Université de Toulouse - UPS, 29 Rue Jeane Marvig, 31055 Toulouse Cedex 4, France

||CAS Key Laboratory of Design and Assembly of Functional Nanostructures, Fujian Key Laboratory of Nanomaterials, Fujian Institute of Research on the Structure of Matter, Chinese Academy of Sciences, Fuzhou, Fujian 350002, China

°Laboratoire de Génie Chimique, CNRS UMR 5503, Université de Toulouse - UPS, 118 route de Narbonne, 31062 Toulouse Cedex 09, France

§BAM Federal Institute of Materials Research and Testing, Division Biophotonics, Richard-Willstätter-Str. 11, D-12489 Berlin, Germany

‡Université de Lille, CNRS, UMR 8516, LASIRE - Laboratoire de Spectroscopie pour les Interactions, la Réactivité et l'Environnement, F-59000 Lille, France

KEYWORDS lanthanide-doped nanoparticles, upconversion, quantum yield, heterostructure, lattice strain, temperature sensing.

ABSTRACT Lanthanide (Ln^{3+})-doped upconversion nanoparticles (UCNPs) often suffer from weak luminescence intensity especially when their sizes are ultrasmall (less than 10 nm). Enhancing the upconversion luminescence (UCL) efficiency of ultrasmall UCNPs has remained a challenge that must be undertaken if any practical applications are to be envisaged. Herein, we present a unique Ln^{3+}-doped oxysulfide@fluoride core/shell heterostructure which shows efficient UCL properties under 980 nm excitation and good stability in solution. Through an epitaxial heterogeneous growth, a ~4 nm optically inert β-$NaYF_4$ shell coats onto ~5 nm ultrasmall Gd_2O_2S:20%Yb,1%Tm. These Gd_2O_2S:20%Yb,1%Tm@$NaYF_4$ core/shell UCNPs show a more than 800-fold increase in UCL intensity compared to the unprotected core, a 200-fold increase in luminescence lifetime of the $^3H_4 \rightarrow {}^3H_6$ Tm^{3+} transition from 5 μs to 1000 μs and an upconversion quantum yield (UCQY) of 0.76% at an excitation power density of 155 W/cm^2. Likewise, Gd_2O_2S:20%Yb,2%Er@$NaYF_4$ core/shell UCNPs show a nearly 5000-fold increase of their UCL intensity compared to the Gd_2O_2S:20%Yb,2%Er core and a maximum UCQY of 0.61%. Further, we have shown that the I_{690}/I_{803} emission of Gd_2O_2S:20%Yb,1%Tm@$NaYF_4$ core/shell UCNPs is very sensitive to temperature. It is likely that this best-in-class relative thermal sensitivity of 3.9% K^{-1} originates from a change in the lattice strain, a property that emanates from the heterogeneous core-shell architecture. Such a result provides a proof-of-concept for the use of these UCNPs for nanothermometry applications.

INTRODUCTION

Lanthanide (Ln^{3+})-doped upconversion nanoparticles (UCNPs) that convert low-energy infrared photons into high-energy ultraviolet (UV) or visible ones have attracted considerable attention in recent decades owing to their unique optical properties such as high photostability, long luminescence lifetimes, and sharp emission bands.[1] These features make UCNPs extremely attractive for use as reporters in fluorescent microscopy, nanomedicine, optogenetics, and nanosensing.[2-7] To date, the major bottlenecks of Ln-based UCNPs reside in the low extinction coefficients of lanthanide ions, together with low upconversion (UC) quantum yield (QY), which, in the case of very small particles, is mostly ascribed to surface quenching effects[8, 9]; the combination of these two factors results in low brightness. Core/shell engineering by addition of an inert shell onto the optically active core, can drastically enhance upconversion luminescence (UCL) efficiency, and has been regarded as the most efficient strategy.[10] To this end, fluoride@fluoride homogeneous (e.g. $NaYF_4$:Yb^{3+},Er^{3+}@$NaYF_4$[11]) or similar (e.g. $NaYF_4$@$NaGdF_4$[12]) core/shell structures have been extensively studied because fluoride host matrices are normally recognized as the most efficient family of host materials with low phonon energies for achieving highly efficient UCL. Construction of heterogeneous core/shell structures by combining two different materials can generally lead to a combination of advantages. For instance, $CsPbBr_3$/$NaYF_4$:Yb,Tm core/shell NPs with extended excitation wavelength to near-infrared (NIR) and improved stability in water due to addition of the fluoride shell, have been synthesized.[13] However, it still remains challenging to synthesize heterostructured nanocrystals consisting of two different families with structural and lattice mismatch.

Rare-earth oxysulfide (RE_2O_2S) materials such as Gd_2O_2S (phonon energy, ~440 cm^{-1}), a family of ideal host materials for Ln^{3+} dopants, have evoked much interest in various

applications due to their wide band-gap, strong antioxidation, high X-ray absorption efficiency, and excellent optical performance.[14-16] Specifically, Gd_2O_2S:Tb based phosphor has been widely used as a highly efficient X-ray scintillator material for intensifier screen, because the emission $^5D_4 \rightarrow {}^7F_5$ of Tb^{3+} under X-ray excitation is located in the green region which matches well with the working range of silicon-based photo-sensors.[17] In addition, Gd_2O_2S:10%Er microcrystals have shown a record-high UCQY value of 12% at 1510 nm infrared (IR) excitation, which makes them suitable for photovoltaic applications.[18] However, because of the limited synthesis strategies, there are no reports of for the fabrication of Gd_2O_2S based heterogeneous core/shell UCNPs with efficient UCL, nor for their application as nanothermometers.

Herein, we present a strategy to construct Ln^{3+}-doped Gd_2O_2S@$NaREF_4$ heterogeneous core/shell structures. An inert $NaYF_4$ shell of ~4 nm thickness was successfully deposited on the ultrasmall (~5 nm) Gd_2O_2S:20%Yb,1%Tm core-only UCNPs. The growth kinetics of RE_2O_2S@$NaREF_4$ core/shell NPs were studied by meticulously analyzing TEM, XRD, and small-angle X-ray scattering (SAXS) in different reaction phases. UCL properties including emission intensity, lifetime, and UCQY of Ln^{3+}-doped Gd_2O_2S@$NaYF_4$ core/shell UCNPs were systematically investigated. Stability of the core-only and core/shell UCNPs in different environments was monitored. Moreover, temperature-dependent UCL spectra and in-situ XRD measurements manifest a correlation between selected emission bands ratio of Er^{3+} and the lattice strain. Finally, we show that Ln^{3+}-doped Gd_2O_2S@$NaREF_4$ core/shell UCNPs have a great capacity for nanothermometry application with highest-in-class thermal sensitivities.

RESULTS AND DISCUSSION

Design and synthesis

Both Gd_2O_2S and $NaYF_4$ are known to have their thermodynamically stable products in a hexagonal lattice, which inspired us to construct a heterogeneous structure Gd_2O_2S@$NaYF_4$. We first theoretically investigated the lattice mismatch between hexagonal RE_2O_2S and $NaREF_4$ (RE = Y, La, Ce, Pr, Nd, Sm, Eu, Gd, Tb, Dy, Ho, Er, Tm, Yb, and Lu). Table S1 shows the identical d-spacings of (101) or (011) planes of RE_2O_2S and (110) or (101) planes of $NaREF_4$, which were extracted from their respective XRD files. The lattice mismatch values were further calculated and given in Table S2. The Gd_2O_2S and $NaYF_4$ lattices show only a mismatch of 0.5%, indicating the feasibility of our concept of Gd_2O_2S@$NaYF_4$ heterostructure formed by epitaxial growth[19, 20] as shown in Figure 1a. A large batch (4 mmol) of Gd_2O_2S:20%Yb,1%Tm core-only UCNPs was first synthesized through a modified thermal decomposition protocol. The preparation of the RE_2O_2S@$NaREF_4$ core/shell NPs was then carried out via high-temperature co-precipitation as previously described[21].

Confirmation of the heterogeneous core/shell structure

The TEM image in Figure S1a shows good dispersity of the as-prepared Gd_2O_2S:20%Yb,1%Tm core-only UCNPs. The corresponding mean size of the NPs was determined to be 5.2 ± 0.9 nm (Figure S1c). The high-resolution (HR) TEM image shows several sets of clear lattice fringes in Figure S1b, indicating the fine crystallinity of the NPs. The d-spacing was measured to be 0.308 nm which can be indexed to (101) lattice plane of Gd_2O_2S. The TEM image in Figure 1b shows highly uniform size and morphology and the HRTEM image in Figure 1c shows good crystallinity of the Gd_2O_2S:20%Yb,1%Tm@$NaYF_4$ core/shell UCNPs. The mean size was determined to be 13.7 ± 0.8 nm in diameter (Figure S2). XRD measurements in Figure S3 confirm the pure hexagonal phase for core-only Gd_2O_2S and the hexagonal $NaYF_4$ for core/shell NPs. It should be noted that the peaks of core/shell NPs shift to the lower 2θ angle, which hints

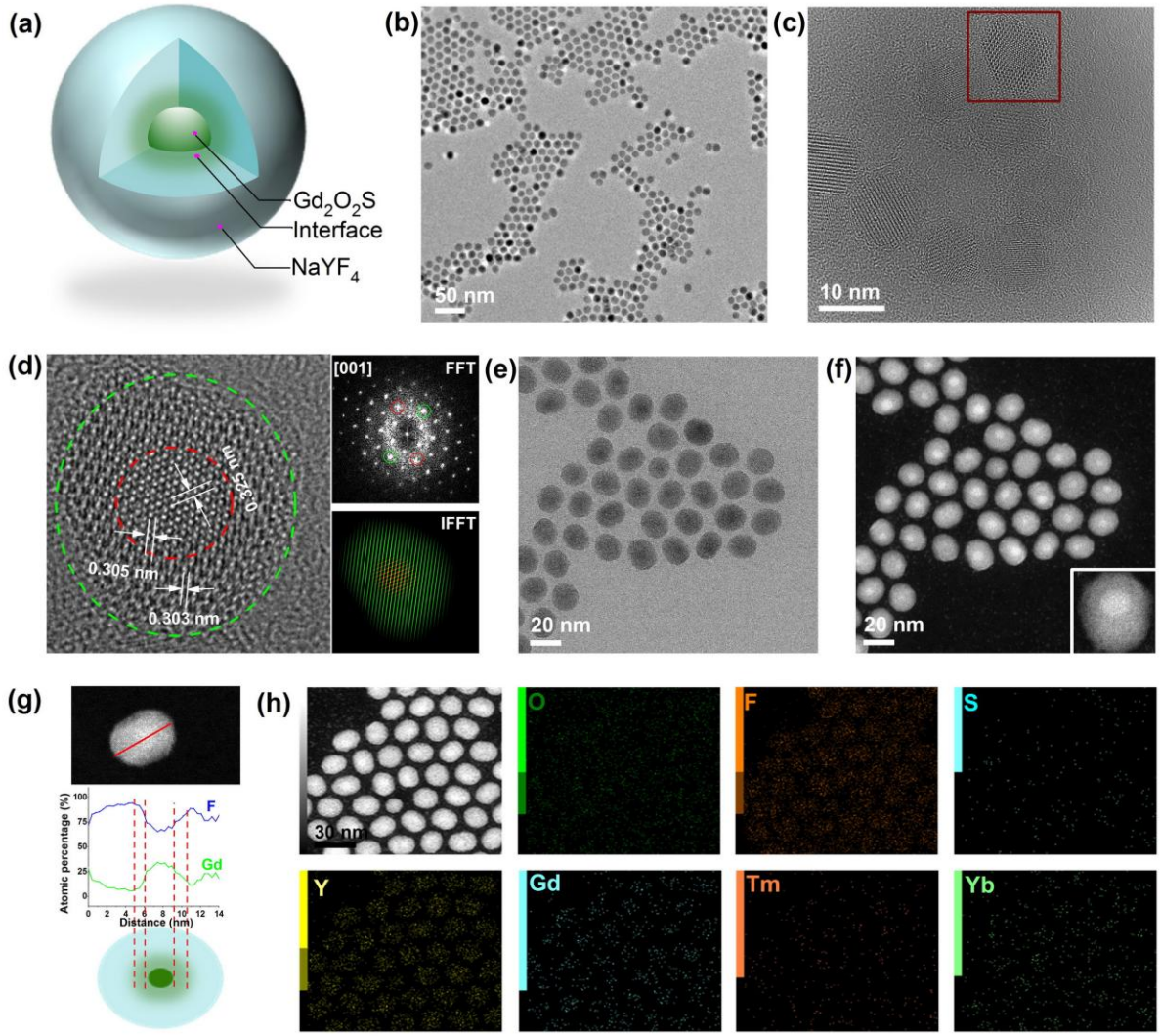

Figure 1. Structure and morphology. (a) Concept graph of Gd_2O_2S@$NaYF_4$ core/shell heterostructure. (b, c) Low- and high- resolution TEM images of Gd_2O_2S:20%Yb,1%Tm@$NaYF_4$ core/shell UCNPs, respectively. (d) HRTEM image of a single nanoparticle extracted from red rectangle of (c), corresponding FFT (top right) and IFFT (bottom right) diffraction patterns showing core (red dashed line) and shell (green dashed line) regions in the nanoparticle. (e, f) ABF and HAADF-STEM images of the core/shell nanoparticles, respectively. (g) Line scan going across a single nanoparticle and the resulting EELS profiles of Gd and F. (h) Element mapping of O, F, S, Y, Gd, Tm, and Yb showing the elemental distribution.

at the lattice distortion in the NPs, however, no obvious Gd_2O_2S diffraction patterns were observed in the XRD of core/shell. We suggest the vanishing of Gd_2O_2S diffraction patterns is

because the very weak diffraction signals of the ultrasmall crystallites are covered by the strong diffraction of the bigger shell. A similar phenomenon has been reported in other heterogeneous α-$NaREF_4$@β-$NaREF_4$ core/shell NPs.[22, 23] To confirm the core/shell structure, a single nanoparticle was extracted from the HRTEM image in Figure 1c, as shown in Figure 1d where we can obviously see two different sets of lattice arrangements: the lattice d-spacings in the center (in the red circle) were measured to be 0.325 nm and 0.305 nm, which respectively correspond to (100) and (101) plane of Gd_2O_2S; and the d-spacing in the out layer (between red and green circles) was determined to be 0.303 nm which corresponds to (110) of $NaYF_4$. The realistic lattice mismatch value of -0.66% between (101) of Gd_2O_2S and (110) of $NaYF_4$ can be easily obtained, which is close to the theoretical prediction based on corresponding bulk materials, indicating that the $NaYF_4$ shell experiences tension. These results imply that the (110) plane of $NaYF_4$ epitaxially grows along the (101) plane of Gd_2O_2S. To further confirm this, we performed fast Fourier transform (FFT) and inverse FFT (IFFT) analysis (Figure 1d right). Two sets of filtered spots (marked as red and green circles) in the FFT pattern were chosen and applied for IFFT. The acquired overlaid IFFT image displays that the red fringes are only from the core region and the green fringes are from shell region matched to core without line defects at the interface. Additionally, Figure S4 shows the HRTEM analyses on another single nanoparticle, where it shows the coherent lattice fringes across the nanoparticle and existence of interface between core and shell. These results, on the one hand, verify our hypothesis of epitaxial growth of the Gd_2O_2S@$NaYF_4$. On the other hand, the existence of strain generated by the lattice mismatch is also verified. The annular bright field (ABF) and high angle annular dark field scanning TEM (HAADF-STEM) images were taken to show the Z-contrast imaging of the NPs. In the HAADF-STEM image (Figure 1f), the brighter areas mainly present the heavier Gd

atoms and darker layers present the lighter Y atoms; inversely, in the ABF image (Figure 1e), the darker grey areas present Gd distribution and the lighter grey areas present Y distribution. In addition, electron energy loss spectroscopy (EELS) in Figure 1g and element mapping images in Figure 1h confirm the composition and the distribution of elements in the Gd_2O_2S:20%Yb,1%Tm@$NaYF_4$ core/shell UCNPs, which are in agreement with previous HRTEM and HAADF measurements, confirming the unique core/shell heterostructure.

Analysis of the growth kinetics

To gain insight into the growth kinetics of Gd_2O_2S:20%Yb,1%Tm@$NaYF_4$ core/shell heterostructure, we performed size and phase evolution investigation based on TEM, XRD, and SAXS characterizations. Samples were collected from the reaction solution after different heating times. TEM images in Figures 2a and S5 show the evolution of size and morphology during the reaction process. From 60 °C to 220 °C (Stage I), we observed one population of well crystallized and uniform NPs with size slightly decreasing with increasing temperature. These NPs were supposedly core-only NPs, maybe some poorly crystallized and small sized α-$NaYF_4$ had been removed during the washing process since it is claimed that α-$NaYF_4$ can be obtained below 220 °C[24]. As the temperature increased, a second population of smaller NPs with a size of 2.8 nm were first observed at 250 °C. These small NPs grew slowly with rising temperature and manifestly disappeared before the 300 °C, 30 min point (end of Stage II). Meanwhile, the size of large NPs increased a little. We assume that the small NPs may be α-$NaYF_4$ as reported previously[25-27], and the large NPs may be the core-only NPs with size enlargement by surface attachments of ultrasmall α-$NaYF_4$. Finally, the large NPs continued to grow and small NPs disappeared as the reaction progressed (Stage III). XRD measurements further confirmed the phase evolution of the NPs. As seen in Figure S6, only the Gd_2O_2S phase was observed before

220 °C but the peaks broadened with increasing temperature due to the formation of smaller size of NPs and a very thin amorphous layer on the surface of the core via the cation exchange process between the core and the precursor solution. This phenomenon is often observed in the synthesis of heterogeneous nanostructures.[28] Subsequently, intense XRD signals of α-$NaYF_4$ phase appeared at 250 °C and overshadowed the intensity of Gd_2O_2S, indicating plenty of α-$NaYF_4$ produced by burst nucleation. With the disappearance of α-$NaYF_4$, the peaks of the β-$NaYF_4$ phase became dominant (Figure S6b).

Based on the above observations and analyses, we concluded a tentative formation process for the Gd_2O_2S:20%Yb,1%Tm@$NaYF_4$ core/shell heterostructure, as shown in Figure 2b. Firstly, cation exchange at the solid-liquid interface can contribute to lowering the interfacial energy of the system, which may form an amorphous layer. Then, with increasing temperature (Stage II), α-$NaYF_4$ nucleation occurs with temperature increases (Stage II). In this stage, ultrasmall α-$NaYF_4$ could be attached on the core-only particles by electrostatic attraction[29], or even form a thin α-$NaYF_4$ layer because some NPs were observed to be more round than before. Since α-

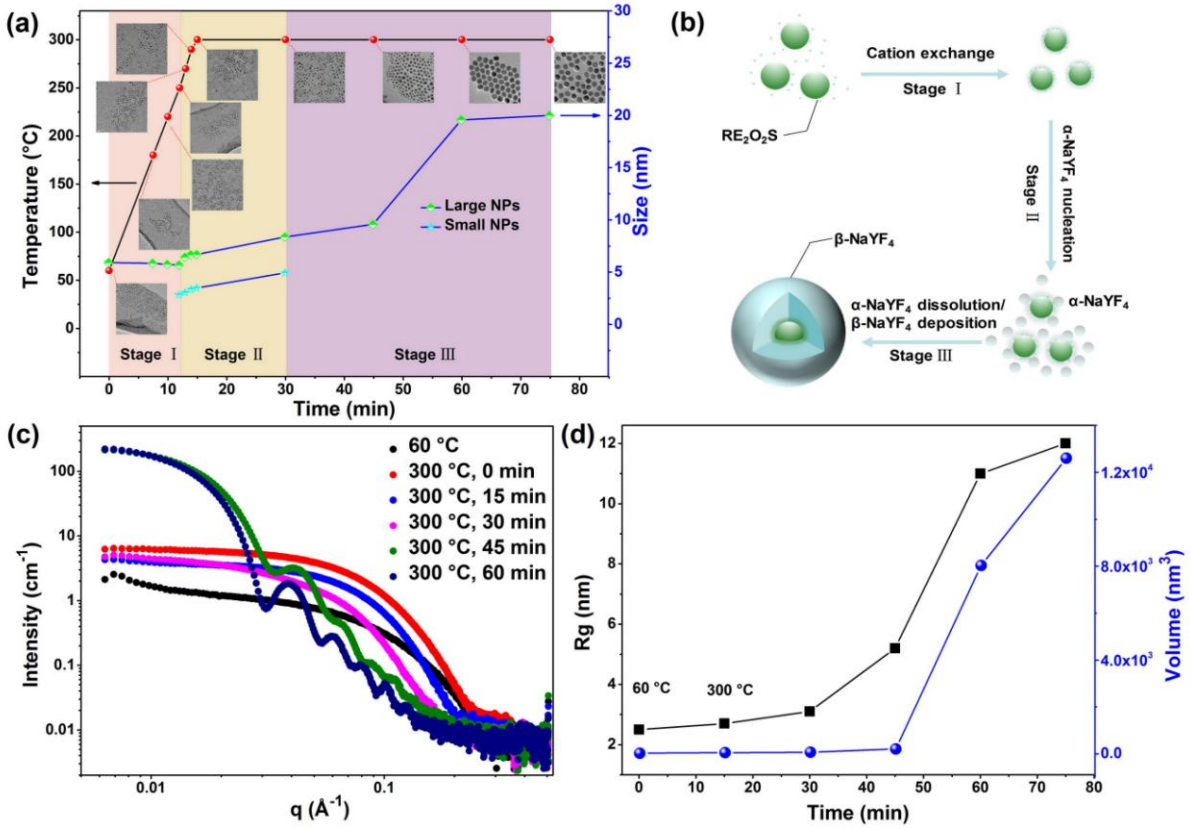

Figure 2. Investigation of growth kinetics. (a) TEM images showing status of nanoparticles at different stages, and sizes evolution during the synthesis. The sizes were statistically measured on at least 50 particles. (b) Proposed formation processes for RE_2O_2S@$NaYF_4$ core/shell heterostructure. (c) SAXS curves for nanoparticles at 60 °C and 300 °C with heating times from 0 to 60 min. (d) Rg and Porod volume extracted from the SAXS data of (c).

$NaYF_4$ is the kinetic product, it dissolves quickly at elevated temperature and nucleates into the thermodynamic β-$NaYF_4$ phase which then deposits on the larger RE_2O_2S NPs (Stage III). Note that this dissolution/deposition process is very rapid. Driven by Ostwald ripening, the larger NPs continually increased in size.

Additionally, SAXS measurements were carried out to investigate global dimensions of the NPs in different reaction phases. As shown in Figure 2c, the superimposition of the SAXS curves shows an increase of the SAXS signal during the temperature rise phase (60 °C *vs.* 300°C, 0 min), suggesting an increase of the concentration of α-$NaYF_4$ NPs. From 0 to 30 min at 300°C, the changes observed on the SAXS curves highlight a phase growth of nanoparticle size. Next, from 45 to 60 min at 300°C, β-$NaYF_4$ phase occurs and grows as demonstrated by the formation of new peaks in the SAXS curves. We noticed that the remarkable modulations in the curves indicate a good monodispersity of the particles in solution. By extracting the data from the SAXS curves, the radius of gyration (Rg) and the Porod volume of particles were determined to follow the particle growth (Figure 2d). It can be seen that the global size increases a little during the temperature rising phase, which is consistent with observation by TEM. In addition, the variations of Rg and volume of particles during the synthesis are in good agreement with the observations by TEM.

The successful preparation of RE_2O_2S@$NaYF_4$ core/shell heterostructure encouraged us to synthesize other heterostructures with different RE-shells. Accordingly, a series of Gd_2O_2S:20%Yb,1%Tm@$NaREF_4$ core/shell NPs (RE = La, Ce, Pr, Nd, Sm, Eu, Gd, Tb, Dy, Ho, Er, Tm, Yb, and Lu) were synthesized by using the same batch of core-only UCNPs. The TEM images in Figure S7 and calculated sizes in Table S3 show the slight variations in shapes and sizes of the core/shell nanoparticles, which are likely caused by the different degrees of lattice

mismatch (ranging from -1.5% to 3.52%, Table S2) between the core and the shell. This establishes the feasibility of core-multishell structures based around oxysulfide cores and paves the way for layered nanocrystals with rational ion segregation.

Enhancement of luminescent properties and stability

The inert $NaYF_4$ shell protects the Ln^{3+}-doped Gd_2O_2S cores from surface quenching, thus significantly boosting the UCL properties. As shown in Figure 3a, under illumination with a continuous wavelength 980 nm laser, Gd_2O_2S:20%Yb,1%Tm core-only and Gd_2O_2S:20%Yb,1%Tm@$NaYF_4$ core/shell UCNPs exhibit emission bands at 469 nm, 640 nm, and 803 nm ascribed to the $^1G_4 \rightarrow {}^3H_6$, $^1G_4 \rightarrow {}^3F_4$, and $^3H_4 \rightarrow {}^3H_6$ transitions of Tm^{3+} (see energy diagram in Figure 4a), respectively. We observed an 836-fold enhancement in overall emission for Tm-doped UCNPs after $NaYF_4$ coating. As a control, we coated the core with a Gd_2O_2S shell using a hot injection method. As shown in Figure S8a, we obtained irregular Gd_2O_2S:20%Yb,1%Tm@Gd_2O_2S core/shell UCNPs with an average size of 14.0 ± 1.4 nm. However, only a 20% luminescence increase was obtained for these Gd_2O_2S:20%Yb,1%Tm@Gd_2O_2S core/shell UCNPs under 980 nm excitation (Figure S8b). This confirms the advantage of a heterogeneous coating for RE_2O_2S UCNPs compared to Gd_2O_2S:20%Yb,1%Tm@Gd_2O_2S homogeneous core/shell UCNPs which displays sub-optimal protections by partial coating, irregular shapes, and a broad size distribution. For Gd_2O_2S:20%Yb,2%Er@$NaYF_4$ core/shell UCNPs, a nearly 5000-fold enhancement was obtained (Figure S9a). Time-resolved luminescence of both Yb^{3+}/Tm^{3+}-doped core-only and core/shell UCNPs were recorded. The lifetimes obtained by a monoexponential fit of the 469 nm and 803 nm emission decays were increased from 8 μs and 5 μs for the core-only (Figure 3b) to 919 μs and 997 μs for the core/shell (Figure 3c), respectively, displaying approximately 100- to

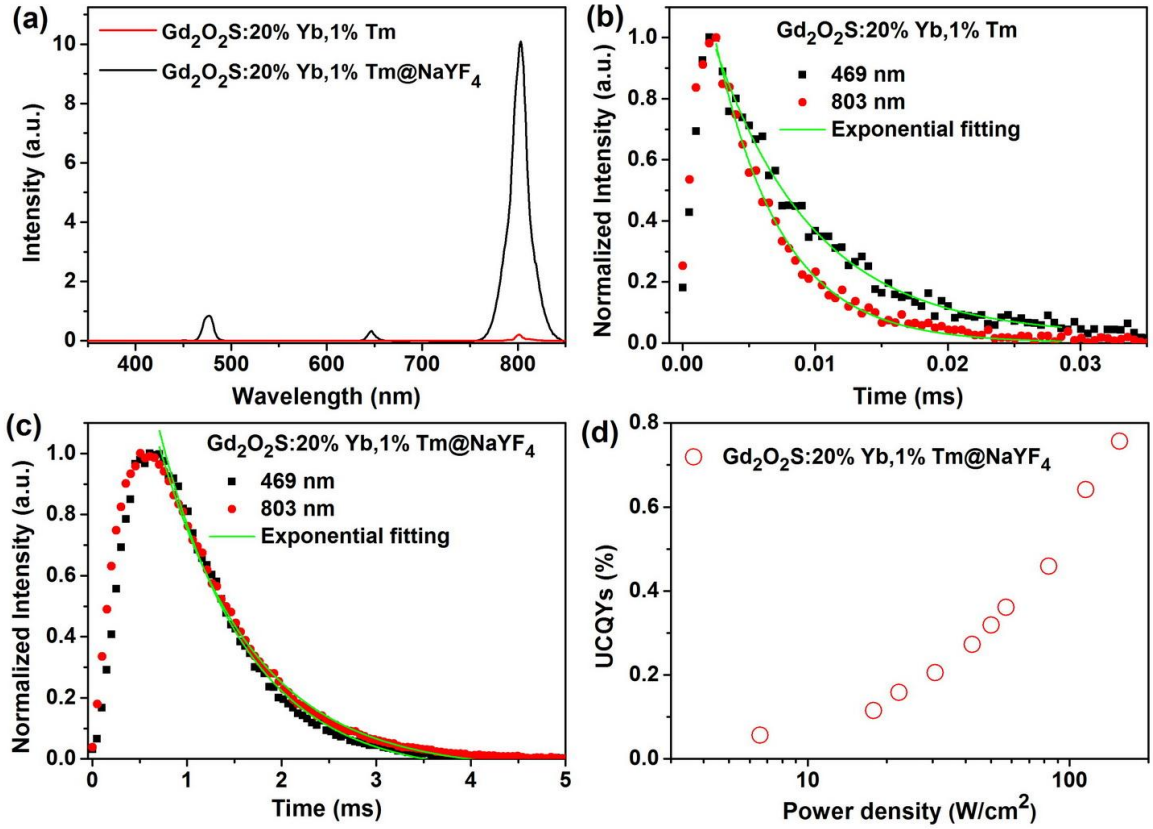

Figure 3. UCL properties. (a) UCL spectra of Gd_2O_2S:20%Yb,1%Tm core-only and Gd_2O_2S:20%Yb,1%Tm@$NaYF_4$ core/shell UCNPs under 980 nm laser excitation. (b, c) UCL decays of core-only and core/shell UCNPs, respectively. (d) Absolutely determined UCQYs of Gd_2O_2S:20%Yb,1%Tm@$NaYF_4$ core/shell UCNPs under different power densities.

200-fold longer lifetimes. The power-dependent absolute UCQYs of the Ln^{3+}-doped Gd_2O_2S@$NaYF_4$ core/shell UCNPs were measured to quantify the UCL efficiency. Figure 3d shows the maximum UCQY value of 0.76% for Gd_2O_2S:20%Yb,1%Tm@$NaYF_4$ at a power density of 155 W/cm^2. Likewise, the maximum UCQY value of 0.61% was acquired for Gd_2O_2S:20%Yb,2%Er@$NaYF_4$ UCNPs (Figure S9b). These UCQYs values are moderate but remarkable considering the very small size of the emitting cores of these UCNPs.[30] In the future, preparing larger core-only NPs or screening proper shell matrices could be attempted to improve the UCQYs.

Although it is claimed that RE_2O_2S materials have good stability[31], however, there is a lack of investigation on the colloidal stability of small-sized and ligand-coated RE_2O_2S NPs. Stability of ligand-coated NPs in various environments (such as cyclohexane, water, and acid solution) plays a vital role in performance characterizations, construction of nanostructures and applications. Hence, we studied the stability of ligand-coated Gd_2O_2S:20%Yb,1%Tm core-only and Gd_2O_2S:20%Yb,1%Tm@$NaYF_4$ core/shell UCNPs in cyclohexane and acidic ethanol solutions. The results in Figures S10 and S11 showed that the core-only UCNPs could not be stably dispersed in cyclohexane at room temperature for a long time without aggregation and they showed low resistance to acidic conditions (acidified ethanol). Comparatively, the core/shell UCNPs with an $NaYF_4$ shell showed good stability in both cyclohexane and acid solution, proving the enhanced stability after coating a fluoride shell.

Temperature effect on the luminescence spectra

Lattice strain in the heterostructure can tune the optical properties of the nanocrystals and can be sensitive to various stimuli such as external mechanical forces and temperature. To verify this, we first implemented temperature-dependent UCL spectra measurements for both Yb^{3+}/Tm^{3+} and Yb^{3+}/Er^{3+} -doped Gd_2O_2S@$NaYF_4$ UCNPs. Figure 4a and Figure S12 show that the UCL intensity increases continuously with increasing temperature from 293 K to 473 K. The intensities of the Tm^{3+} bands at 469 nm, 640 nm, 690 nm ($^3F_{2,3} \rightarrow {}^3H_6$), and 803 nm were 3, 2, 10, and 3 times higher at 473 K than those at 293 K, respectively (Figure 4b). Notably, the reason for the greater enhancement of the 690 nm band is that $^3H_4$ and $^3F_{2,3}$ energy levels are thermally-coupled, thus favoring the population at the higher level of $^3F_{2,3}$ at an elevated temperature. This indicates that the UCNPs have a high sensitivity to temperature and thus can be good candidates as thermometers. A similar thermal enhancement was observed for the UCL of Yb^{3+}/Er^{3+}-doped

Gd_2O_2S@$NaYF_4$ UCNPs, shown in Figures 4c, S13, and 4d. As the temperature increases, the intensities of the Er^{3+} peaks at 520 nm ($^2H_{11/2} \rightarrow {}^4I_{15/2}$), 540 nm ($^4S_{3/2} \rightarrow {}^4I_{15/2}$), and 652 nm ($^4F_{9/2} \rightarrow {}^4I_{15/2}$) increase by factors of 3.9, 1.1, and 2.8 at 473 K compared to those at 293 K.

In recent years, thermally enhanced UCL has attracted a lot of attention and several hypotheses such as surface phonon assistance[32], surface molecule desorption[33], and energy transfer suppression induced by lattice expansion[34] have been proposed. In our case, the shell thickness of small (< 30 nm) Gd_2O_2S@$NaYF_4$ core/shell UCNPs is only about 4 nm which cannot completely prevent surface quenching by water molecules. Hence, we thought that the UCL enhancement with increasing temperature in our UCNPs was caused by water desorption[4, 33, 35]. To confirm this hypothesis, we carried out heating-cooling cycle experiments for Gd_2O_2S:20%Yb,2%Er@$NaYF_4$ core/shell UCNPs. As shown in Figure S14, in the first 2 cycles, thermal UCL enhancement was observed as the temperature increased. However, the UCL intensity continued to increase in the cooling process, which could be due to water desorption. In the last 3 cycles, the UCL intensity at 473 K was always higher than that at 293 K, which means surface attached water molecules were almost removed and thermal quenching was dominant.

Apart from the UCL enhancement, the intensity ratio of I_{652}/I_{540} changed as a function of

temperature. Figure 4e shows that the ratio first increases linearly from 293 K to 423 K, then

remains almost stable from 423 K to 463 K, and finally drops at 473 K. The ratio at 423 K is

165% higher than that at 293 K. As we know, the variation of $^4S_{3/2} \rightarrow {}^4F_{9/2}$ non-radiative

relaxation can influence the I_{652}/I_{540} ratios. Here two factors should be taken into account:

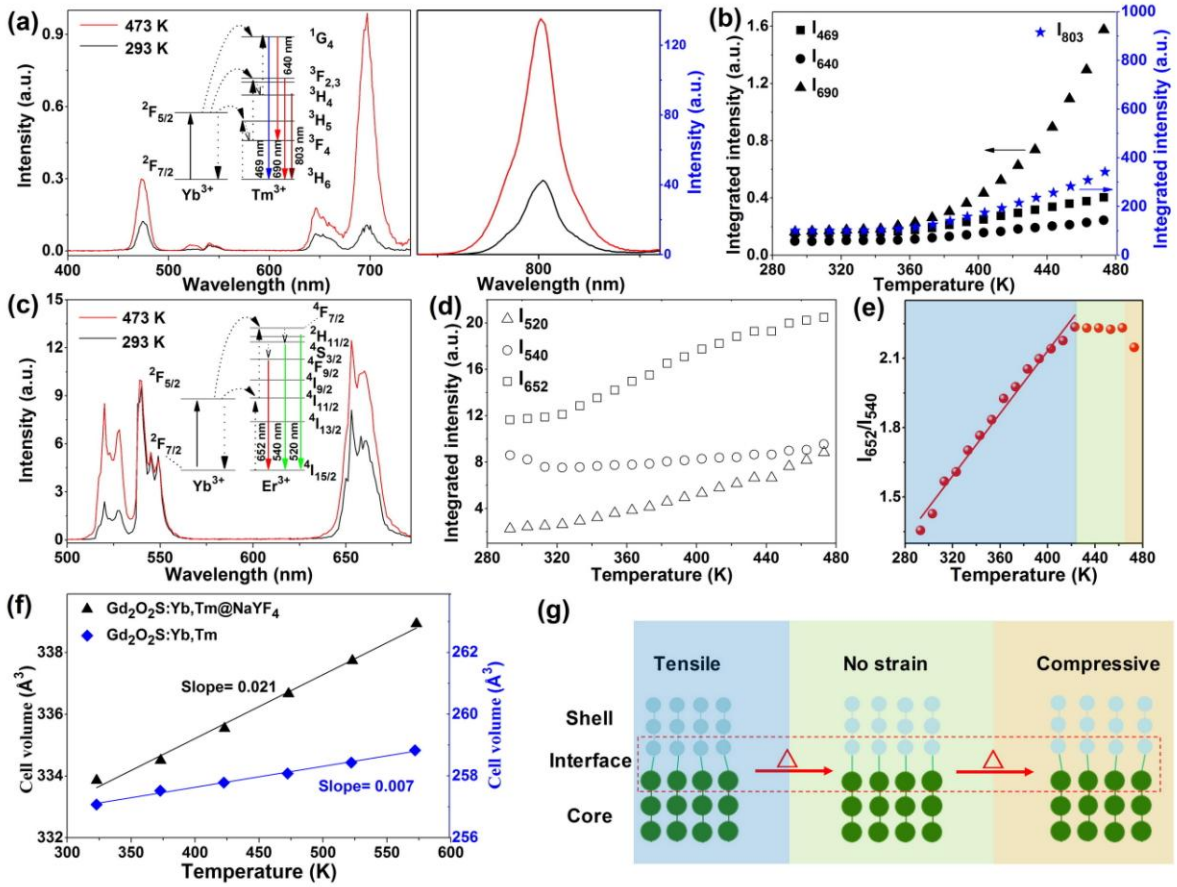

Figure 4. Analyses of temperature-dependent UCL spectra. (a, b) Variation of UCL spectra and integrated intensities of the peaks of Tm^{3+}, respectively, of Gd_2O_2S:20%Yb,1%Tm@$NaYF_4$ core/shell UCNPs with increasing temperature. Inset energy level diagram shows the upconversion mechanism of Tm^{3+} ions. (c, d) Variation of UCL spectra and integrated intensities of the peaks of Er^{3+}, respectively, of Gd_2O_2S:20%Yb,2%Er@$NaYF_4$ core/shell UCNPs with increasing temperature. Inset energy level diagram shows the upconversion mechanism of Er^{3+} ions. (e) Temperature-dependent red/green emission intensity ratios (I_{652}/I_{540}) of Gd_2O_2S:20%Yb,2%Er@$NaYF_4$ core/shell UCNPs. The red straight line is plotted by linear fitting in the temperature range of 293~423 K. (f) Cell volume as a function of temperature plots for both core and core/shell compositions. The thermal volume expansion rates can be determined by linearly fitting the respective data points. (g) Schematic illustration of lattice distortion variation with increasing temperature. It shows that the lattice distortion will vary from tensile strain to compressive strain due to large differences in thermal expansion rates of plane spacings between core and shell materials.

heating and differential lattice expansion. An increasing temperature can enhance the non-

radiative relaxation of the $^4S_{3/2} \rightarrow {}^4F_{9/2}$ transition, leading to an increase of the I_{652}/I_{540} ratio. This can, however, only explain the change in the first temperature range from 293 K to 423 K. As the temperature continues to rise, the I_{652}/I_{540} ratio nearly remains constant and even drops at 473 K. Hence, lattice expansion seems to be involved as well. We first carried out in-situ XRD measurements at different temperatures (from 323 K to 573 K) for both core-only and core/shell UCNPs, as shown in Figures S15 and S16. To ensure the reversibility of the lattice constants after heating process, the XRD patterns of the UCNPs were measured twice at 323 K. Note the Gd_2O_2S:Yb,Tm core-only UCNPs were synthesized by a solid state method to avoid surface ligands and used as a reference[36], and the surface ligand of Gd_2O_2S:Yb,Tm@$NaYF_4$ core/shell UCNPs were removed by an acid treatment method (see Supporting Information). The lattice constants were determined by Pawley method fitting[37], then the cell volumes at different temperatures were calculated (see Tables S4 and S5). Further, the linear fitting of cell volume versus temperature plots revealed thermal volume expansion rates of 0.007 $Å^3$/K and 0.021 $Å^3$/K for Gd_2O_2S:Yb,Tm core-only and Gd_2O_2S:Yb,Tm@$NaYF_4$ core/shell, respectively (Figure 4f).

Based on the previous XRD and HRTEM analyses, existence of tensile strain in the $NaYF_4$ shell has been confirmed at ambient temperature. Therefore, we could postulate the variation of the interface lattice distortion with elevating temperature as illustrated in Figure 4g. The lattice distortion decreases with elevating temperature because of the large difference of the expansion rate between core and shell (shell expansion rate is 300% higher than core) and reach an equilibrium. This process has recently been reported as lattice self-adaptation[38]. It is inferred that further increasing the temperature would generate compressive strain in the shell. The varied strain in the shell generates opposite strain in the core, producing variation in the local structure in the interfacial area, further changing the optical properties of such heterostructures.[39] When

the temperature increases from 293 to 423 K, decrease of compressive strain in the core leads to enhancement of $^4S_{3/2} \rightarrow {}^4F_{9/2}$ non-radiative transition, linearly increasing the luminescence intensity ratio I_{652}/I_{540}, which is in a good agreement with investigations of the Er^{3+} emission of other $NaYF_4$ based heterostructures subjected to heating[40] and mechanical forces[41, 42]. Then, the I_{652}/I_{540} ratio remains nearly constant in the range of 423~463 K due to zero strain at the interfacial area. Finally, the inverse tensile strain in the core decreases the I_{652}/I_{540} ratio at 473 K. Importantly, when the lattice strain at the interface has a strong influence on the population of thermally-coupled emissive states, it can be harnessed to enhance the sensitivity to temperature.[38, 40, 41]

Towards a nanothermometry probe

As a proof-of-concept, we demonstrated a high response of UCL to temperature change using our custom-designed Ln^{3+} doped Gd_2O_2S@$NaREF_4$ heterostructures. Since 980 nm excited $^3F_{2,3} \rightarrow {}^3H_6$ (I_{690}) and $^3H_4 \rightarrow {}^3H_6$ (I_{803}) of Tm^{3+}, $^2H_{11/2} \rightarrow {}^4I_{15/2}$ (I_{520}) and $^4S_{3/2} \rightarrow {}^4I_{15/2}$ (I_{540}) of Er^{3+} UCL (arising from their respective thermally coupled energy levels) comply with Boltzmann distribution theory[43, 44], the luminescence intensity ratio (LIR) can be expressed following the equation:

$$LIR = \frac{I_2}{I_1} = Cexp^{(-\Delta E/kT)} \qquad (1)$$

where I_2 and I_1 corresponds to the integrated fluorescence intensities of high-energy level and low-energy level, respectively; C is a constant; ΔE is the energy gap; k is the Boltzmann constant and T is the absolute temperature. The obtained LIR and Ln(LIR) values were fitted with Eq. (1) for Yb^{3+}/Tm^{3+} and Yb^{3+}/Er^{3+} doped Gd_2O_2S@$NaYF_4$ core/shell UCNPs respectively, as shown in Figures 5a and 5d (the fitting results can be found in the Supporting Information).

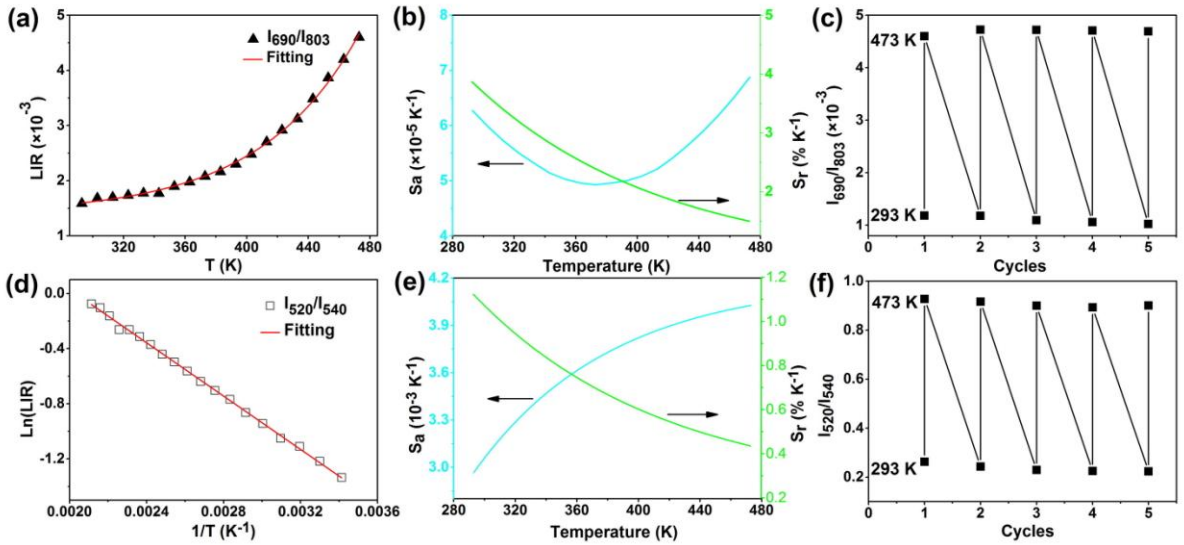

Figure 5. Thermal sensitivity. (a) LIR vs T, (b) dependence of absolute (S_a) and relative (S_r) thermal sensitivity on temperature, and (c) heating-cooling cycles for I_{690}/I_{803} of Gd_2O_2S:20%Yb,1%Tm@$NaYF_4$ core/shell UCNPs. (d) Ln(LIR) vs 1/T, (e) dependence of S_a and relative S_r on temperature, and (f) heating-cooling cycles for I_{520}/I_{540} of Gd_2O_2S:20%Yb,2%Er@$NaYF_4$ core/shell UCNPs.

To further evaluate the temperature sensing behavior of our UCNPs, the absolute thermal sensitivity (S_a) and the relative temperature sensitivity (S_r) were calculated using the following equations[43, 44]:

$$S_a = \frac{\partial LIR}{\partial T} = LIR\left(\frac{\Delta E}{kT^2}\right) \qquad (2)$$

$$S_r = \frac{1}{LIR}\frac{\partial LIR}{\partial T} = \left(\frac{\Delta E}{kT^2}\right) \qquad (3)$$

The S_a and S_r values for both Yb^{3+}/Tm^{3+} and Yb^{3+}/Er^{3+} doped UCNPs have been presented in Figures 5b and 5e. As can be seen, the Yb^{3+}/Tm^{3+} doped UCNPs exhibit the maximum S_a at 473 K with 0.0069% K^{-1} and S_r at 293 K with 3.9% K^{-1}; the Yb^{3+}/Er^{3+} doped UCNPs exhibit the maximum S_a at 473 K with 0.4% K^{-1} and S_r at 293 K with 1.1% K^{-1}. We performed the same method to assess the temperature sensing capacity for Gd_2O_2S:20%Yb,1%Tm@$NaLuF_4$ UCNPs

which has a different shell coating matrix, as shown in Figure S17. The maximum S_a at 473 K with 3.0% K^{-1} and S_r at 293 K with 3.3% K^{-1} were obtained for the UCNPs. To assess the photochemical stability of our luminescent nanoprobes, we performed 5 heating-cooling cycles for both Yb^{3+}/Tm^{3+} and Yb^{3+}/Er^{3+} doped UCNPs. According to the data in Figure 5c and 5f, the reproducibility value (R) was calculated to be higher than 95% by the method reported previously[7].

Table 1 summarizes the sensitivities obtained from other previously reported material systems using the same intensity ratios of Tm^{3+} and Er^{3+} for comparison. It can be found that the maximum S_r of our Gd_2O_2S:20%Yb,1%Tm@$NaYF_4$ core/shell UCNPs is the highest amongst Yb^{3+}/Tm^{3+} doped systems, and even the $NaLuF_4$-coating UCNPs have a greater S_r value than previously reported Lu-based materials in the same temperature range reported in the literature[45]. Also, the Yb^{3+}/Er^{3+} doped Gd_2O_2S@$NaYF_4$ core/shell UCNPs have an excellent maximum S_r value which is comparable with the values found for other systems. The increased performance of the thermal sensitivity of our UCNPs seems to be associated with interfacial lattice strain that can enhance the temperature sensitivity. Note that all the compositions of our NPs in this study are still not optimized towards temperature sensitivity, which further highlights the potential of Ln^{3+} doped RE_2O_2S@$NaREF_4$ as a new kind of luminescence-based nanothermometer.

Table 1. Comparison of the relative thermal sensitivities (S_r) of Yb/Tm or Yb/Er doped systems in the similar temperature range. Luminescence intensity ratios (LIR) from the transitions $^3F_{2,3} \rightarrow {}^3H_6/{}^3H_4 \rightarrow {}^3H_6$ for Tm^{3+} and $^2H_{11/2} \rightarrow {}^4I_{15/2}/{}^4S_{3/2} \rightarrow {}^4I_{15/2}$ for Er^{3+} under 980 nm laser excitation.

Material	T-range (K)	FIR	Sr (% K^{-1})	Ref.
Gd_2O_2S:Yb,Tm@$NaYF_4$	293-473	I_{690}/I_{803}	3.9 at 293 K	This work
Gd_2O_2S:Yb,Tm@$NaLuF_4$	293-473	I_{690}/I_{803}	3.3 at 293 K	This work
$GdYO_4$:Yb,Tm@SiO_2	298-333	I_{700}/I_{800}	3.3 at 298 K	[46]

$LiNbO_3$:Yb,Tm	323-773	I_{700}/I_{800}	3.0 at 323 K	[47]
$NaYbF_4$:Tm	298-778	I_{697}/I_{803}	1.9[#] at 298 K	[48]
$NaBiF_4$:Yb,Tm	303-443	I_{697}/I_{800}	2.7[#] at 303 K	[49]
$KLuF_4$:Yb,Tm	303-503	I_{690}/I_{795}	1.4[#] at 303 K	[45]
Gd_2O_2S:Yb,Er@$NaYF_4$	293-473	I_{520}/I_{540}	1.1 at 293 K	This work
$(NaGdF_4$:Er/$NaYF_4)_n$	298-348	I_{520}/I_{539}	3.0 at 298 K	[38]
$NaLuF_4$:Yb,Er,Ho	298-503	I_{524}/I_{547}	0.74 at 298K	[50]
β-$NaYF_4$:Yb,Er@SiO_2	299-337	I_{525}/I_{545}	1.3 at 299 K	[51]
Gd_2O_3:Yb,Er	300-900	I_{523}/I_{548}	0.8[#] at 300 K	[52]
$NaYF_4$:Yb,Er	293-333	I_{525}/I_{545}	1.2[#] at 293 K	[53]

[#] Values determined by us for this study, according to the data published by the authors in the original literature.

CONCLUSIONS

In conclusion, we have designed an upconversion core/shell heterostructure by combining RE_2O_2S and $NaREF_4$ matrices formed by heterogeneous epitaxial deposition mechanism as demonstrated by growth kinetic studies. Upon addition of inert $NaREF_4$ shells, we observed remarkable improvements of the UCL intensities, lifetimes, and UCQYs, as well as stability for the core/shell UCNPs compared to those features of the cores. These results confirmed the effective protection brought by the shell to the core not only in the UCL properties but also the enhanced stability in different solvent environments. The distortion at the core/shell interface induced by lattice mismatch was observed by HRTEM and XRD analyses. For both Yb^{3+}/Er^{3+} and Yb^{3+}/Tm^{3+} doped Gd_2O_2S@$NaYF_4$ core/shell UCNPs, the temperature-induced lattice distortion provides the ability to design sensitive optical probes response to temperature and mechanical forces. In addition, tunable interfacial strain by varying shell components may give possibilities to further improve the sensitivities. The Yb^{3+}/Tm^{3+} doped Gd_2O_2S@$NaYF_4$

nanoprobes exhibits a relative thermal sensitivity of 3.9% K^{-1}, the highest reported yet in this range of temperature, to the best of our knowledge. Taken together, our findings provide a new basis for upconversion heterostructures and open up pathways to other combinations of hexagonal rare-earth oxysulfides and sodium rare-earth fluorides.

METHODS

Detailed experimental procedures for synthesis of core-only and core/shell NPs are provided in the Supporting Information.

ASSOCIATED CONTENT

Supporting Information. Complete nanoparticle synthesis and characterization description. Additional XRD of core and core/shell NPs, size summary of NPs, lattice parameters and lattice mismatch values determined from ICDD data, in-situ XRD, TEM images, UCL spectra, temperature-dependent UCL spectra, thermal sensitivity determination of Gd_2O_2S:20%Yb,1%Tm@$NaLuF_4$ core/shell UCNPs; including Tables S1-S5, Figures S1-S15 (PDF).

AUTHOR INFORMATION

Corresponding Authors

*c.roux@chimie.ups-tlse.fr

*robert.mauricot@cemes.fr

*xchen@fjirsm.ac.cn

Author Contributions

Q.Z.: investigation, data curation, formal analysis and manuscript writing. C.M.: investigation. N.R.R.: investigation. X.Y.: investigation. P.R.: investigation. F.F.: investigation. U.R.G.: funding acquisition. A.E.: investigation. A.B.: investigation, funding acquisition. C.C.: formal analysis. M.V.: formal analysis. X.C.: funding acquisition and writing. R.M.: project administration, funding acquisition and writing. C.R.: project administration, funding acquisition and writing.

Notes

The authors declare no competing financial interest.

ACKNOWLEDGMENTS

We are grateful to Dr. W. Zheng, Dr. M. Sliwa, Dr. C. Würth, and Dr J-C Micheau for the fruitful discussions. Q. Zou acknowledges the support from the French Research ministry in the form of a PhD scholarship and the DAAD short-term grant from German government. X. Chen acknowledges the support from the NSFC (No. U1805252) and the CAS/SAFEA International Partnership Program for Creative Research Teams. We thank the federation FERMAT of Toulouse for giving us access to the SAXS bench.

REFERENCES

1. Haase, M.; Schäfer, H., Upconverting Nanoparticles. *Angew. Chem. Int. Ed.* **2011,** *50* (26), 5808-5829.

2. Zheng, K.; Loh, K. Y.; Wang, Y.; Chen, Q.; Fan, J.; Jung, T.; Nam, S. H.; Suh, Y. D.; Liu, X., Recent advances in upconversion nanocrystals: Expanding the kaleidoscopic toolbox for emerging applications. *Nano Today* **2019,** *29*.

3. Wen, S.; Zhou, J.; Schuck, P. J.; Suh, Y. D.; Schmidt, T. W.; Jin, D., Future and challenges for hybrid upconversion nanosystems. *Nat. Photon.* **2019,** *13* (12), 828-838.

4. Chen, B.; Wang, F., Emerging Frontiers of Upconversion Nanoparticles. *Trends Chem.* **2020,** *2* (5), 427-439.

5. All, A. H.; Zeng, X.; Teh, D. B. L.; Yi, Z.; Prasad, A.; Ishizuka, T.; Thakor, N.; Hiromu, Y.; Liu, X., Expanding the Toolbox of Upconversion Nanoparticles for In Vivo Optogenetics and Neuromodulation. *Adv. Mater.* **2019,** *31* (41), 1803474.

6. Qiu, X.; Zhou, Q.; Zhu, X.; Wu, Z.; Feng, W.; Li, F., Ratiometric upconversion nanothermometry with dual emission at the same wavelength decoded via a time-resolved technique. *Nat. Comm.* **2020,** *11*, 4.

7. Brites, C. D. S.; Balabhadra, S.; Carlos, L. D., Lanthanide-Based Thermometers: At the Cutting-Edge of Luminescence Thermometry. *Adv. Opt. Mater.* **2019,** *7*, 1801239.

8. Zheng, W.; Huang, P.; Tu, D.; Ma, E.; Zhu, H.; Chen, X., Lanthanide-doped upconversion nano-bioprobes: electronic structures, optical properties, and biodetection. *Chem. Soc. Rev.* **2015,** *44* (6), 1379-1415.

9. Li, X.; Zhang, F.; Zhao, D., Highly efficient lanthanide upconverting nanomaterials: Progresses and challenges. *Nano Today* **2013,** *8* (6), 643-676.

10. Su, Q.; Han, S.; Xie, X.; Zhu, H.; Chen, H.; Chen, C.-K.; Liu, R.-S.; Chen, X.; Wang, F.; Liu, X., The Effect of Surface Coating on Energy Migration-Mediated Upconversion. *J. Am. Chem. Soc.* **2012,** *134* (51), 20849-20857.

11. Homann, C.; Krukewitt, L.; Frenzel, F.; Grauel, B.; Würth, C.; Resch-Genger, U.; Haase, M., $NaYF_4$:Yb,Er/$NaYF_4$ Core/Shell Nanocrystals with High Upconversion Luminescence Quantum Yield. *Angew. Chem. Int. Ed.* **2018,** *57*, 8765 –8769.

12. Abel, K. A.; Boyer, J.-C.; Veggel, F. C. J. M. v., Hard Proof of the $NaYF_4$/$NaGdF_4$ Nanocrystal Core/Shell Structure. *J. Am. Chem. Soc.* **2009,** *131* (41), 14644-14645.

13. Ruan, L.; Zhang, Y., NIR-excitable heterostructured upconversion perovskite nanodots with improved stability. *Nat. Comm.* **2021,** *12*.

14. Zhang, P.; Liang, L.; Liu, X., Lanthanide-doped nanoparticles in photovoltaics – more than just upconversion. *J. Mater. Chem. C* **2021**.

15. Ludwig, G. W.; Prener, J. S., Evaluation of Gd_2O_2S:Tb as a Phosphor for the Input Screen of X-Ray Image Intensifier. *IEEE Trans. Nucl. Sci.* **1972,** *19* (4), 3-8.

16. Qian, B.; Wang, D.; Wang, H.; Zou, H.; Song, Y.; Zhou, X.; Sheng, Y., Solvothermal synthesis of columnar $Gd_2O_2S:Eu^{3+}$ and a comparative study with columnar $Gd_2O_3:Eu^{3+}$. *J. Am. Ceram. Soc.* **2020,** *103* (1), 356-366.

17. Machado, I. P.; Teixeira, V. C.; Pedroso, C. C. S.; Brito, H. F.; Rodrigues, L. C. V., X-ray scintillator $Gd_2O_2S:Tb^{3+}$ materials obtained by a rapid and cost-effective microwave-assisted solid-state synthesis. *J. Alloys Compd.* **2019,** *777*, 638-645.

18. Martín-Rodríguez, R.; Fischer, S.; Ivaturi, A.; Froehlich, B.; Krämer, K. W.; Goldschmidt, J. C.; Richards, B. S.; Meijerink, A., Highly Efficient IR to NIR Upconversion in $Gd_2O_2S: Er^{3+}$ for Photovoltaic Application. *Chem. Mater.* **2013,** *25*, 1912−1921.

19. Ronny Costi; Saunders, A. E.; Banin, U., Colloidal Hybrid Nanostructures: A New Type of Functional Materials. *Angew. Chem. Int. Ed.* **2010,** *49*, 4878-4897.

20. Carbonea, L.; Cozzoli, D., Colloidal heterostructured nanocrystals: Synthesis and growth mechanisms. *Nano Today* **2010,** *5*, 449-493.

21. Qian, H.-S.; Zhang, Y., Synthesis of Hexagonal-Phase Core-Shell $NaYF_4$ Nanocrystals with Tunable Upconversion Fluorescence. *Langmuir* **2008,** *24*, 12123-12125.

22. Chen, H.; Zhang, P.; Cui, H.; Qin, W.; Zhao, D., Synthesis and Luminescence Properties of Water Soluble α-$NaGdF_4$/β-$NaYF_4$:Yb,Er Core–Shell Nanoparticles. *Nanoscale Res. Lett.* **2017,** *12*, 548.

23. Shao, Q.; Yang, C.; Chen, X.; Zhang, H.; Feng, G.; Zhou, S., Core-mediated synthesis, growth mechanism and near-infrared luminescence enhancement of α-$NaGdF_4$@β-$NaLuF_4$:Nd^{3+} core–shell nanocrystals. *CrystEngComm* **2020,** *22*, 1359-1367.

24. Naccache, R.; Yu, Q.; Capobianco, J. A., The Fluoride Host: Nucleation, Growth, and Upconversion of Lanthanide-Doped Nanoparticles. *Adv. Opt. Mater.* **2015,** *3*, 482-509.

25. Peng, X.; Schlamp, M. C.; Kadavanich, A. V.; Alivisatos, A. P., Epitaxial Growth of Highly Luminescent CdSe/CdS Core/Shell Nanocrystals with Photostability and Electronic Accessibility. *J. Am. Chem. Soc.* **1997,** *119*, 7019-7029.

26. Peng, X.; Wickham, J.; Alivisatos, A. P., Kinetics of II-VI and III-V Colloidal Semiconductor Nanocrystal Growth: "Focusing" of Size Distributions. *J. Am. Chem. Soc.* **1998,** *120*, 5343-5344.

27. Johnson, N. J. J.; Korinek, A.; Dong, C.; Veggel, F. C. J. M. v., Self-Focusing by Ostwald Ripening: A Strategy for Layer-by-Layer Epitaxial Growth on Upconverting Nanocrystals. *J. Am. Chem. Soc.* **2012,** *134*, 11068−11071.

28. Zhao, D.; Chen, H.; Zheng, K.; Chuai, X.; Yu, F.; Li, H.; Wu, C.; Qin, G.; Di, W.; Qin, W., Growth of hexagonal phase sodium rare earth tetrafluorides induced by heterogeneous cubic phase core. *RSC Adv.* **2014,** *4*, 13490–13494.

29. Chen, X.; Peng, D.; Ju, Q.; Wang, F., Photon upconversion in core–shell nanoparticles. *Chem. Soc. Rev.* **2015,** *44*, 1318-1330.

30. Würth, C.; Fischer, S.; Grauel, B.; Alivisatos, A. P.; Resch-Genger, U., Quantum Yields, Surface Quenching, and Passivation Efficiency for Ultrasmall Core/Shell Upconverting Nanoparticles. *J. Am. Chem. Soc.* **2018,** *140*, 4922-4928.

31. Larquet, C.; Carenco, S., Metal Oxysulfides: From Bulk Compounds to Nanomaterials. *Front. Chem.* **2020,** *8*, 179.

32. Zhou, J.; Wen, S.; Liao, J.; Clarke, C.; Tawfik, S. A.; Ren, W.; Mi, C.; Wang, F.; Jin, D., Activation of the surface dark-layer to enhance upconversion in a thermal field. *Nat. Photon.* **2018,** *12*, 154-158.

33. Hu, Y.; Shao, Q.; Dong, Y.; Jiang, J., Energy Loss Mechanism of Upconversion Core/Shell Nanocrystals. *J. Phys. Chem. C* **2019,** *123*.

34. Cui, X.; Cheng, Y.; Lin, H.; Huang, F.; Wu, Q.; Wang, Y., Size-dependent abnormal thermo-enhanced luminescence of ytterbium-doped nanoparticles. *Nanoscale* **2017,** *9*, 13794–13799.

35. Shi, R.; Martinez, E. D.; Brites, C. D. S.; Carlos, L. D., Thermal enhancement of upconversion emission in nanocrystals: a comprehensive summary. *Phys. Chem. Chem. Phys.* **2021,** *23*, 20-42.

36. Osseni, S. A.; Lechevallier, S.; Verelst, M.; Perriat, P.; Dexpert-Ghys, J.; Neumeyer, D.; Garcia, R.; Mayer, F.; Djanashvili, K.; Peters, J. A.; Magdeleine, E.; Gros-Dagnac, H.; Celsis, P.; Mauricot, R., Gadolinium oxysulfide nanoparticles as multimodal imaging agents for T_2-weighted MR, X-ray tomography and photoluminescence. *Nanoscale* **2014,** *6*, 555–564.

37. Pawley, G., Unit-cell refinement from powder diffraction scans. *J. Appl. Cryst.* **1981,** *14* (6), 357-361.

38. Wu, X.; Zhan, S.; Han, J.; Liu, Y., Nanoscale Ultrasensitive Temperature Sensing Based on Upconversion Nanoparticles with Lattice Self-Adaptation. *Nano Lett.* **2021,** *21* (1), 272-278.

39. Bao, H.; Wang, W.; Li, X.; Liu, X.; Zhang, L.; Yan, X.; Wang, Y.; Wang, C.; Jia, X.; Sun, P.; Kong, X.; Zhang, H.; Lu, G., Interfacial Stress-Modulated Mechanosensitive

Upconversion Luminescence of $NaErF_4$ Based Heteroepitaxial Core–Shell Nanoparticles. *Adv. Opt. Mater.* **2022,** *10* (2), 2101702.

40. Zhao, J.; Chen, X.; Chen, B.; Luo, X.; Sun, T.; Zhang, W.; Wang, C.; Lin, J.; Su, D.; Qiao, X.; Wang, F., Accurate Control of Core–Shell Upconversion Nanoparticles through Anisotropic Strain Engineering. *Adv. Funct. Mater.* **2019,** *1903295*.

41. Lay, A.; Siefe, C.; Fischer, S.; Mehlenbacher, R. D.; Ke, F.; Mao, W. L.; Alivisatos, A. P.; Goodman, M. B.; Dionne, J. A., Bright, Mechanosensitive Upconversion with Cubic-Phase Heteroepitaxial Core−Shell Nanoparticles. *Nano Lett.* **2018,** *18*, 4454−4459.

42. Lay, A.; Wang, D. S.; Wisser, M. D.; Mehlenbacher, R. D.; Lin, Y.; Goodman, M. B.; Mao, W. L.; Dionne, J. A., Upconverting Nanoparticles as Optical Sensors of Nano- to MicroNewton Forces. *Nano Lett.* **2017,** *17*, 4172−4177.

43. Wade, S. A.; Collins, S. F.; Baxter, G. W., Fluorescence intensity ratio technique for optical fiber point temperature sensing. *J. Appl. Phys.* **2003,** *94*, 4743-4756.

44. Bradac, C.; Lim, S. F.; Chang, H.-C.; Aharonovich, I., Optical Nanoscale Thermometry: From Fundamental Mechanisms to Emerging Practical Applications. *Adv. Opt. Mater.* **2020,** *8*, 2000183.

45. Min, Q.; Bian, W.; Qi, Y.; Lu, W.; Yu, X.; Xu, X.; Zhou, D.; Qiu, J., Temperature sensing based on the up-conversion emission of Tm^{3+} in a single $KLuF_4$ microcrystal. *J. Alloys Compd.* **2017,** *728*, 1037-1042.

46. Savchuk, O.; Marti, J. J. C.; Cascales, C.; Haro-Gonzalez, P.; Diaz, F.; Sanz-Rodríguez, F.; Aguilo, M., Bifunctional Tm^{3+},Yb^{3+}:$GdVO_4$@SiO_2 Core-Shell Nanoparticles in HeLa Cells: Upconversion Luminescence Nanothermometry in the First Biological Window and Biolabelling in the Visible. *Nanomaterials 2020, 10, 993* **2020,** *10*, 993.

47. Xing, L.; Xu, Y.; Wang, R.; Xu, W.; Zhang, Z., Highly sensitive optical thermometry based on upconversion emissions in Tm^{3+}/Yb^{3+} codoped $LiNbO_3$ single crystal. *Opt. Lett.* **2014,** *39*, 454-457.

48. Lei, L.; Zhang, S.; Xia, H.; Tian, Y.; Zhang, J.; Xua, S., Controlled synthesis of lanthanide-doped Gd_2O_2S nanocrystals with a novel excitation-dependent multicolor emissions. *Nanoscale* **2017,** *9*, 5718-5724.

49. Tian, X.; Dou, H.; Wu, L., Photoluminescence and thermometry properties of upconversion phosphor $NaBiF_4$: Yb^{3+}/Tm^{3+}. *Opt. Mater.* **2020,** *99*, 109544.

50. Runowskia, M.; Bartkowiaka, A.; Majewskaa, M.; Martínb, I. R.; Lisa, S., Upconverting lanthanide doped fluoride $NaLuF_4:Yb^{3+}$-Er^{3+}-Ho^{3+} - optical sensor for multi-range fluorescence intensity ratio (FIR) thermometry in visible and NIR regions. *J. Lumin.* **2018,** *201*, 104-109.

51. Runowski, M.; Stopikowska, N.; Szeremeta, D.; Goderski, S.; Skwierczyńska, M.; Lis, S., Upconverting Lanthanide Fluoride Core@Shell Nanorods for Luminescent Thermometry in the First and Second Biological Windows: β-$NaYF_4:Yb^{3+}$ − $Er^{3+}@SiO_2$ Temperature Sensor. *ACS Appl. Mater. Interfaces* **2019,** *11*, 13389−13396.

52. Singh, S. K.; Kumar, K.; Rai, S. B., Er^{3+}/Yb^{3+} codoped Gd_2O_3 nano-phosphor for optical thermometry. *Sens. Actuators A Phys.* **2009,** *149*, 16-20.

53. Vetrone, F.; Naccache, R.; Zamarrón, A.; Fuente, A. J. d. l.; Sanz-Rodríguez, F.; Maestro, L. M.; Rodriguez, E. M.; Jaque, D.; Solé, J. G.; Capobianco, J. A., Temperature Sensing Using Fluorescent Nanothermometers. *ACS Nano* **2010,** *4*, 3254–3258.